

# Quantification of ion scattering by solar wind current sheets: Pitch-angle diffusion rates

Zjin Zhang

Anton Artemyev

Vassilis Angelopoulos

2025-07-23

Because solar wind plasma flow transports the entire spectrum of magnetic field fluctuations (from low-frequency inertial range to electron kinetic range), it is a natural laboratory for plasma turbulence investigation. Among the various wave modes and coherent plasma structures that contribute to this spectrum, one of the most important solar wind elements is the ion-scale solar wind discontinuities. These structures, which carry very intense current, have been considered as a free energy source for plasma instabilities that contribute to solar wind heating. Investigations of such discontinuities have been mostly focused on their magnetic field signatures; much less is known about their role in scattering of energetic ions. In this study, we consider an observational-based model of ion dynamics and scattering in force-free rotational magnetic discontinuities. Focusing on quantification of the scattering effect, we demonstrate that the background sheared magnetic field plays an important role in determining the efficiency of pitch angle scattering. We provide a model including statistical properties of solar wind discontinuities and providing estimates of ion scattering rate.

## Note

This document and the accompanying website contain outdated information. Please refer to the [published paper](#) for the accurate and updated information.

## Introduction

The transport of energetic particles within the heliosphere is significantly influenced by the turbulent magnetic field present in the solar wind [[Giacalone and Jokipii, 1999](#), [Pucci et al., 2016](#)]. Rather than being a simple superposition of random fluctuations, these turbulent fields exhibit a structured nature, frequently observed in solar wind data in the form of current sheets, discontinuities, Alfvén vortices, magnetic holes, and other coherent structures [[Perrone](#)

et al., 2020, 2016]. These structures arise from nonlinear energy cascade processes [De Giorgio et al., 2017, Meneguzzi et al., 1981] and play a critical role in modulating particle transport. Specifically, current sheets—often manifesting as rotational discontinuities—act as efficient scatterers in collisionless plasmas [Artemyev et al., 2020, Malara et al., 2021]. Understanding the interaction between energetic particles and such coherent structures is essential for accurately modeling particle transport in the heliosphere [Desai and Giacalone, 2016] and has fundamental implications for particle acceleration at interplanetary shock waves [Lee and Fisk, 1982].

Despite extensive research on solar wind turbulence, the quantitative impact of coherent structures on particle transport remains insufficiently explored. Previous studies have primarily focused on idealized turbulence models [Giacalone and Jokipii, 1999, Matthaeus et al., 2003], often neglecting the specific role of coherent structures such as current sheets. This study aims to bridge this gap by providing a detailed analysis of particle interactions with current sheets using a simplified analytical model of the magnetic field configuration, incorporating realistic statistical parameters derived from solar wind observations at 1 AU. By leveraging an exact Hamiltonian formulation that accounts for the rotational effects of the magnetic field, alongside test particle simulations, we investigate the evolution of particle pitch angle and the statistical long-term behavior of pitch-angle scattering across different particle energies. This approach allows us to extend prior works [see review about energetic particles modelling Whitman et al., 2023, and references therein] by incorporating realistic coherent structures.

The structure of this paper is as follows: In Section , we present a detailed description of the magnetic field model and the fundamental equations governing particle motion. In Section , we introduce the concept of adiabatic invariance and discuss its violations due to separatrix crossings. Section presents numerical simulation results and statistical observations of current sheets in the solar wind. In Section , we analyze the long-term evolution of particle pitch angles due to multiple scatterings by current sheets. Finally, a discussion and conclusions are provided in Section .

## Basic Equations

We assume the following 1-D force-free magnetic field configuration where  $\mathbf{B}$  depends only on the  $z$  coordinate:

$$\mathbf{B} = B(\cos \theta \mathbf{e}_z + \sin \theta (\sin \varphi(z) \mathbf{e}_x + \cos \varphi(z) \mathbf{e}_y))$$

where  $B$  is the magnitude of the magnetic field,  $\theta$  is the azimuthal angle between the normal  $\mathbf{B}_z = B \cos \theta \mathbf{e}_z \equiv B_n \mathbf{e}_z$  and the magnetic field. More specifically we assume the following form,  $\varphi(z) = \beta \tanh(z/L)$ , where  $L$  is the thickness of the current sheet and shear angle  $\beta$  is the half of in plane rotation angle  $\omega_{in}$ . The transverse magnetic field component  $\mathbf{B}_t = B_t \sin \varphi(z) \mathbf{e}_x + B_t \cos \varphi(z) \mathbf{e}_y$  rotates by an angle  $\omega_{in}$  from  $-\infty$  to  $+\infty$  where  $B_t = B \sin \theta$ . As an example, we present an observation from the ARTEMIS mission [Angelopoulos, 2011],

which captures a magnetic field transition consistent with our model. Figure 1 shows the variations in  $\mathbf{B}$ ,  $\theta$ , and  $\varphi$  across the current sheet. The transverse field rotates smoothly, with  $\varphi$  following a hyperbolic tangent profile (note that time is linearly proportional to the spatial coordinate  $z \approx v_n t$  where  $v_n$  is the solar wind velocity along the normal to the current sheet surface), while  $\theta$  remains nearly constant near  $\pi/2$ , indicating a small normal component  $B_n$ . (A three-dimensional visualization of a typical current sheet magnetic field structure, represented by the magnetic field line, together with three representative particle trajectories is provided in Figure 5.)

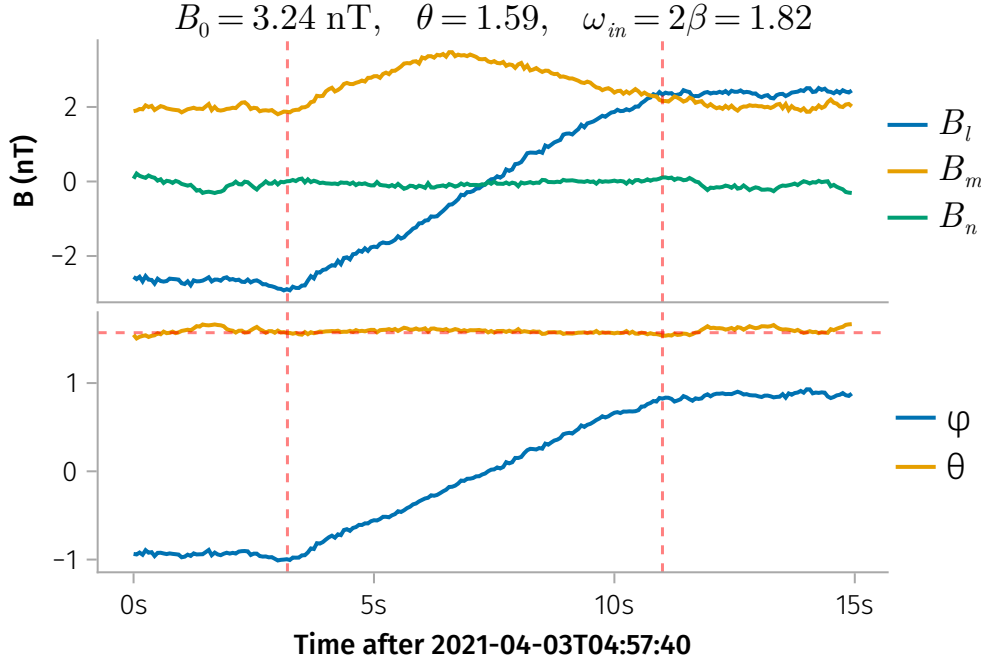


Figure 1: Example of a current sheet observed by ARTEMIS [Angelopoulos, 2011]. Top: magnetic field in the current sheet **lmn** coordinate system [Sonnerup and Scheible, 1998] where  $l$  represents the maximum variance direction ( $B_x = B_t \sin \varphi$  in our model),  $m$  the intermediate variance direction ( $B_y = B_t \cos \varphi$ ), and  $n$  the minimum variance direction ( $B_z = B \cos \theta$ ). Here,  $B_t$  and  $B$  represent the tangential and total magnetic fields, respectively (see text for detailed definitions). Bottom: variations of the azimuthal angle  $\varphi$  and the azimuthal angle  $\theta$  across the current sheet. Vertical lines indicate the current sheet boundaries, and the horizontal line represents  $\pi/2$ . The analysis is based on magnetic field data with a 0.25-second resolution from the Fluxgate Magnetometer [Auster et al., 2008].

The motion of a particle in such a field can be expressed in the Hamiltonian formalism as follows:

$$H = \frac{1}{2m} (\mathbf{p} - q\mathbf{A})^2$$

where  $\mathbf{A}$  represents the magnetic vector potential,  $\mathbf{p}$  is the canonical momentum. More specifically, the magnetic vector potential  $\mathbf{A}$  can be expressed in an exact integrable form:

$$\begin{aligned} A_x &= LB_t f_1(z) \\ A_y &= LB_t f_2(z) + xB_n \\ A_z &= 0 \end{aligned}$$

$$\begin{aligned} f_1(z) &= \frac{1}{2} \cos \beta \left( \text{Ci} \left( \beta + \beta \tanh \left( \frac{z}{L} \right) \right) - \text{Ci} \left( \beta - \beta \tanh \left( \frac{z}{L} \right) \right) \right) + \frac{1}{2} \sin \beta \left( \text{Si} \left( \beta + \beta \tanh \left( \frac{z}{L} \right) \right) - \text{Si} \left( \beta - \beta \tanh \left( \frac{z}{L} \right) \right) \right) \\ f_2(z) &= \frac{1}{2} \sin \beta \left( \text{Ci} \left( \beta + \beta \tanh \left( \frac{z}{L} \right) \right) + \text{Ci} \left( \beta - \beta \tanh \left( \frac{z}{L} \right) \right) \right) - \frac{1}{2} \cos \beta \left( \text{Si} \left( \beta + \beta \tanh \left( \frac{z}{L} \right) \right) + \text{Si} \left( \beta - \beta \tanh \left( \frac{z}{L} \right) \right) \right) \end{aligned}$$

We introduce a dimensionless Hamiltonian  $\tilde{H} = H/h$  by normalizing  $(x, z) = (\tilde{x}L + c_x, \tilde{z}L)$  and  $(p_x, p_z) = p(\tilde{p}_x, \tilde{p}_z)$  where  $p = \frac{qLB_t}{c}$  and  $h = \frac{q^2L^2B_t^2}{mc^2}$ . Note that because  $\partial H/\partial y = 0$ ,  $p_y = \text{const}$  and we could let  $c_x = \frac{cp_y}{qB_n}$  to eliminate  $p_y$ :

$$\tilde{H} = \frac{1}{2} \left( (\tilde{p}_x - f_1(z))^2 + (\tilde{x} \cot \theta + f_2(z))^2 + \tilde{p}_z^2 \right)$$

It is important to note that this is an exact Hamiltonian of the particle dynamics. We do not expand it near the neutral plane  $z = 0$  like previous study employing the Hamiltonian formalism [Artemyev et al., 2020]. This Hamiltonian also accounts for the rotational effect  $\beta$ . By expanding the Hamiltonian near the current sheet to third order and assuming  $\beta = 1$ , it can be reduced to the form used in [Artemyev et al., 2020], where  $\kappa = \cot \theta$ . In this study, we quantitatively investigate the influence of shear angle ( $\beta$ ) and particle energy ( $E$ ) on the efficiency of pitch-angle scattering. For simplicity, the tilde notation over dimensionless variables is omitted in the following discussion.

## Adiabatic invariance and its violations at separatrix crossings

For discontinuities where  $B_n/B_t \ll 1$ , the variables  $(\kappa x, p_x)$  evolve significantly more slowly compared to  $(z, p_z)$ . Assuming that  $x$  and  $p_x$  are effectively frozen, the Hamiltonian describes a periodic motion within the  $(z, p_z)$  plane, governed by the effective potential energy  $U(z) = H - p_z^2$ . When variations in  $(\kappa x, p_x)$  occur on a timescale much longer than the fast oscillations in  $(z, p_z)$ , the generalized magnetic moment  $I_z = (2\pi)^{-1} \oint p_z dz$  is conserved as an adiabatic invariant with exponential accuracy [Neishtadt, 2000].

This Hamiltonian supports two distinct types of ion motion in the  $(z, p_z)$  plane, as illustrated in Figure 2. In the left portrait, there are two potential wells, resulting in one or two possible orbits in the  $(z, p_z)$  plane depending on the value of  $H$ . In contrast, the right portrait represents a case with only one possible orbit in the  $(z, p_z)$  plane for a fixed  $H$ . As  $(\kappa x, p_x)$  evolve slowly, the particle's trajectory in the  $(z, p_z)$  plane undergoes a gradual transformation. Transitions between motion types can occur, accompanied by significant trajectory reconfigurations when the particle crosses the separatrix. Near the separatrix, the instantaneous period of motion increases logarithmically, diverging as the trajectory approaches it. When the timescales of fast oscillations and variations in the control parameter become comparable, the particle accumulates a nonvanishing change in the adiabatic invariant, resulting in a jump in  $I_z$  of approximately  $\sim 1$ . This jump arises primarily from the geometrical destruction of adiabatic invariance [Artemyev et al., 2020], and corresponds to the difference in areas enclosed by the separatrix in the  $(z, p_z)$  plane which is independent of  $\kappa$ . Concurrently, the projection of the particle's phase point onto the  $(\kappa x, p_x)$  plane lies along the so-called uncertainty curve, which demarcates regions corresponding to different types of motion in the  $(z, p_z)$  plane.

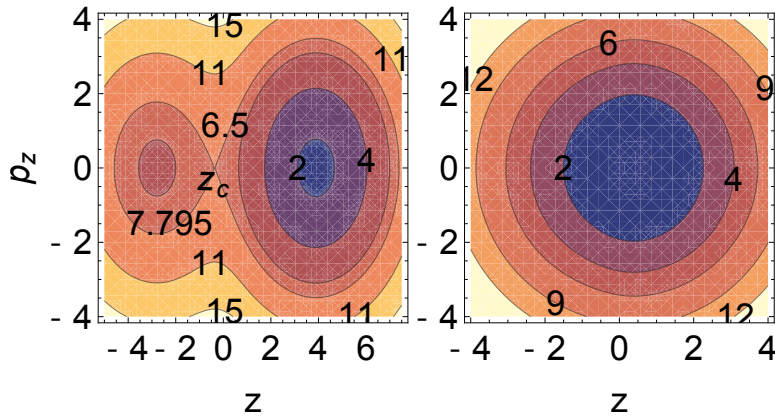


Figure 2: Phase portraits of Hamiltonian at frozen  $(\kappa x, p_x)$  for  $\beta = 1$ :  $H$  values of each curve are shown in the plot;  $\kappa x = 4, p_x = 1$  in the left panel and  $\kappa x = 0, p_x = 0.5$  in the right panel.

Due to the symmetry of ion motion about the  $p_z = 0$  line, the potential energy  $U$  reaches a local maximum along the  $z$ -direction at the saddle point  $z = z_c, p_z = 0$  where two lobes connect. At this point, the conditions  $\partial U / \partial z = 0$  and  $\partial^2 U / \partial z^2 < 0$  are satisfied. These conditions allow the expression of the slow variables along the uncertainty curve in the  $(\kappa x, p_x)$  plane as functions of  $z_c$ . When a particle trajectory crosses the  $z = 0$  plane, the crossing point is confined within a circular region defined by  $(p_x - f_1(0))^2 + (\kappa x + f_2(0))^2 = 2H$ . The likelihood of the trajectory intersecting the uncertainty curve is therefore proportional to the uncertainty curve length  $L_{uc}$ , normalized by the square root of the particle energy,  $\sqrt{H}$ , as illustrated in Figure 3. For fixed  $H$ ,  $L_{uc}/\sqrt{H}$  increases with  $\beta$ , indicating higher scattering probabilities at larger magnetic field rotation angles. Similarly, at a fixed  $\beta$ ,  $L_{uc}/\sqrt{H}$  increases with  $H$ , suggesting that high-energy ions are more susceptible to pitch-angle scattering.

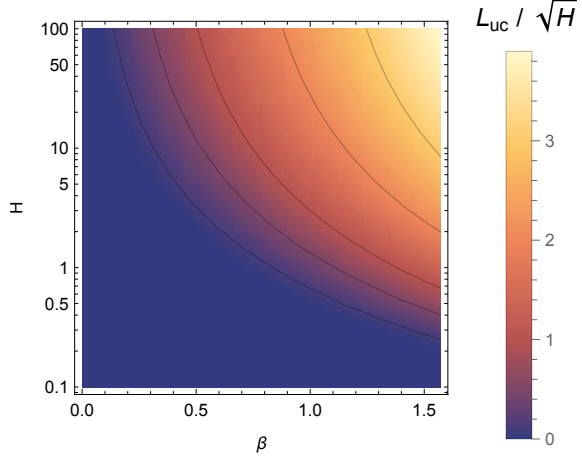


Figure 3: Density plot of the uncertainty curve length  $L_{uc}/\sqrt{H}$  as a function of  $\beta$  and normalized particle energy  $H$ , overlaid with constant contour curves.

## Test particle simulations

To quantitatively analyze how particles are scattered by solar wind discontinuities, we conducted extensive test particle simulations using a dataset of solar wind current sheets at 1 AU. Since the primary focus is on protons, the particle mass was set to  $m_p$  (proton mass) and the charge to the elementary charge  $q$ . According to the dimensionless Hamiltonian, the critical current sheet parameters influencing particle dynamics are the angles  $\theta$  and  $\beta = \omega_{in}/2$ , along with the parameter  $B_t L$ , which appears in the dimensionless factor  $h = \frac{q^2 L^2 B_t^2}{mc^2}$ . By applying a simple transformation,  $B_t = B_0 \sin \theta$ , the key current sheet parameters become  $\theta$ ,  $\omega_{in}$ , and  $v_0 = \Omega_0 L = qB_0 L/(cm_p)$ , where  $\Omega_0$  is the gyrofrequency associated with the magnetic field  $B_0$ .

Using data from the Wind mission, we compiled a dataset of 100,000 discontinuities. The orientations of these discontinuities were determined using the minimum variance analysis of the magnetic field (MVAB) method. Accurate orientation determination was crucial for estimating the discontinuities' thickness ( $L$ ) and the in-plane magnetic field rotation angle ( $\omega_{in}$ ), both of which significantly influence ion scattering. To ensure reliability, only discontinuities with  $\Delta|B|/|B| > 0.05$  or  $\omega > 60^\circ$  were used in the following analysis, as these conditions improve the accuracy of the MVAB method, as noted by [Liu et al. \[2023\]](#). The two parameters  $\Delta|B|/|B| > 0.05$  and  $\omega > 60^\circ$  are independent of the discontinuity normal and can be calculated directly from magnetic field data. Figure 4 shows 3D density plots of the azimuthal angle  $\theta$ , the in-plane rotation angle  $\omega_{in}$ , and the logarithm of the characteristic velocity  $\log v_0$ , categorized by whether the accuracy conditions are satisfied (left for not accurate, right for accurate). Current sheets with accurately determined orientations typically have smaller azimuthal angles  $\theta$ , indicating a smaller  $B_n$ , and moderate in-plane rotation angles  $\omega_{in}$ . In contrast, current

sheets with potentially inaccurate normal orientations display larger  $\theta$  (larger  $B_n$ ) and larger  $\omega_{in}$ . The most probable values observed in the distribution are a characteristic velocity ( $v_0$ ) of approximately 500 km/s, an in-plane rotation angle ( $\omega_{in}$ ) near 100 degrees, and an azimuthal angle ( $\theta$ ) around 85-95 degrees.

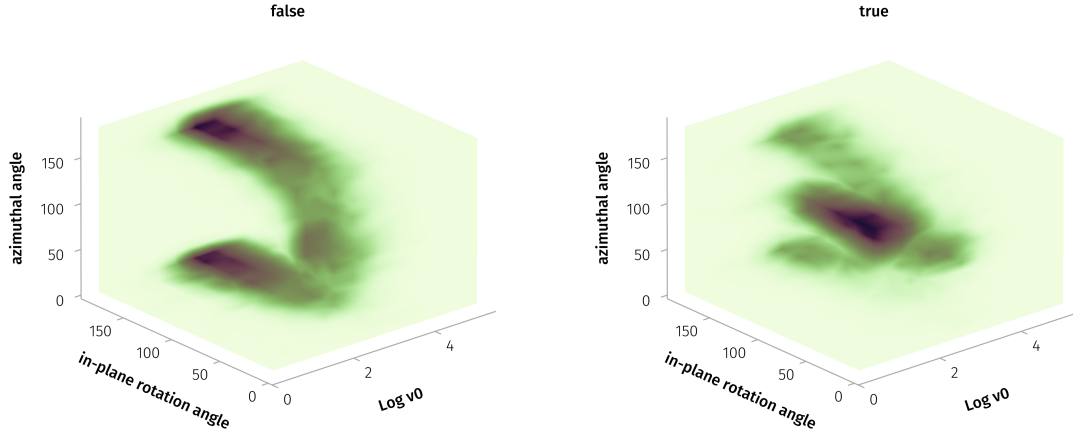


Figure 4: 3D density plots of the azimuthal angle  $\theta$ , in-plane rotation angle  $\omega_{in}$ , and logarithm of the characteristic velocity  $\log v_0$ . The left panel corresponds to cases where the accuracy conditions are not satisfied, while the right panel represents cases where they are satisfied.

For each magnetic field configuration, we initialize an ensemble of particles far away from the current sheet center (i.e., with an initial  $z$  position satisfying  $|z_0| > 6L + 2r_g$ , where  $r_g$  is the gyro radius). The particles are uniformly binned in pitch angle ( $\alpha_0$ ) from  $0^\circ$  to  $180^\circ$  in 180 bins of size  $\Delta\alpha = 1^\circ$ , with gyro phase ( $\psi_0$ ) uniformly sampled from  $0^\circ$  to  $360^\circ$  in 120 bins of size  $\Delta\psi = 3^\circ$ . In this simulation, the current sheet is consistently configured with a positive  $B_z$  component. Consequently, particles with an initial positive pitch-angle cosine  $\mu \equiv \cos \alpha$  ( $\alpha_0 < 90^\circ$ ;  $\mu_0 > 0$ ) are interpreted to originate below the current sheet (and move toward the current sheet), while those with a negative cosine ( $\alpha_0 > 90^\circ$ ;  $\mu_0 < 0$ ) are considered to come from above it (and move toward the current sheet). The particle trajectories are then numerically integrated until each particle fully exits the current sheet ( $|z(t)| > |z_0| + 2r_g$ ). Figure 5 shows three representative particle trajectories in a typical magnetic field configuration characterized by  $\beta = 75^\circ$  and  $\theta = 85^\circ$ . All particles have the same initial pitch angle  $\alpha_0 = 90^\circ$  and velocity  $v_p = 8v_B$ , but differ slightly in their initial gyrophases:  $\phi_0 = 163.3^\circ, 164.4^\circ$ , and  $165.6^\circ$ . These cases illustrate distinct scattering behaviors: one particle exhibits a negligible change in pitch angle, another undergoes a finite pitch-angle deflection, and the third is reflected by the current sheet. For each trajectory, the final pitch angle  $\alpha_1$  is recorded. These pitch angles are then organized into bins to construct a transition matrix (TM), also known as a stochastic matrix [Durrett, 2016], which represents the probability distribution of pitch-angle

changes resulting from a single particle interaction with the current sheet.

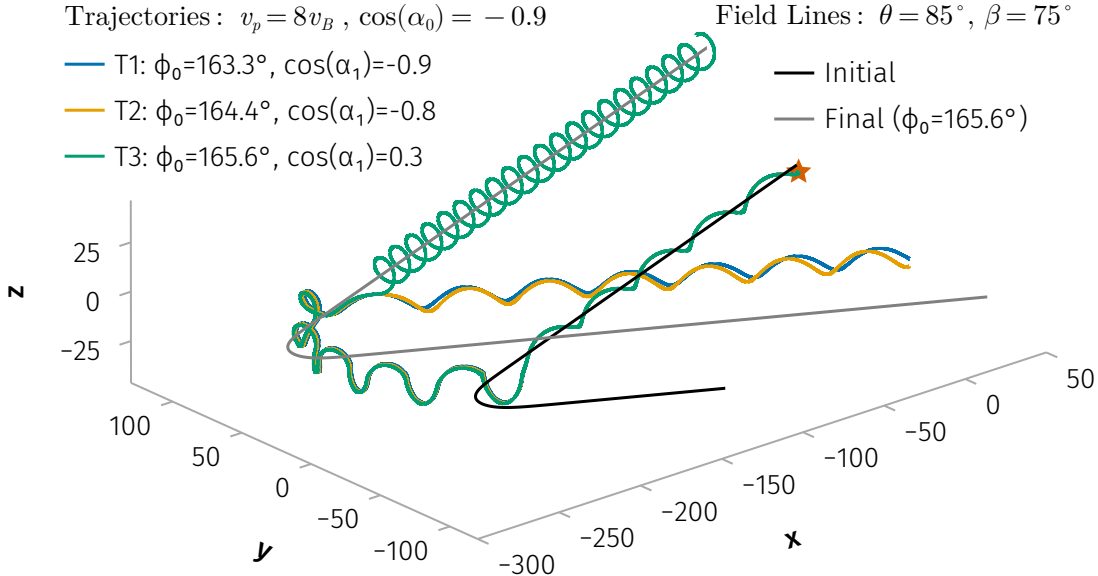


Figure 5: Three particle trajectories (T1, T2, T3) with identical initial pitch angles ( $\alpha_0 = 90^\circ$ ) and velocity  $v_p = 8v_B$ , but slightly different initial gyrophases ( $\phi_0 = 163.3^\circ, 164.4^\circ, 165.6^\circ$ ) in a representative magnetic field profile ( $\beta = 75^\circ, \theta = 85^\circ$ ). The orange star marks the initial particle position. The black and gray lines represent the magnetic field lines to which the reflected particle (T3) is initially and finally attached, respectively, before and after interaction with the current sheet.

Figure 6 illustrates the transition matrix for 100 keV particles (velocity  $v_p \approx 4000$  km/s) under four magnetic field configurations: (i)  $v_0 = 500$  km/s,  $\theta = 85^\circ$ ,  $\beta = 50^\circ$ ; (ii)  $v_0 = 500$  km/s,  $\theta = 85^\circ$ ,  $\beta = 75^\circ$ ; (iii)  $v_0 = 500$  km/s,  $\theta = 60^\circ$ ,  $\beta = 50^\circ$ ; and (iv)  $v_0 = 4000$  km/s,  $\theta = 85^\circ$ ,  $\beta = 50^\circ$ . Enhanced probability along the diagonal corresponds to weakly scattered particles ( $\Delta\alpha = \alpha_1 - \alpha_0 = 0$ ), while spreading around the diagonal reflects diffusive scattering. Large pitch-angle jumps are represented by non-diagonal elements.

The transition matrix profiles for various current sheet configurations reveal that particle pitch-angle evolution during multiple current sheet crossings is influenced by a combination of weak/strong diffusion and large jumps. For instance, in current sheets with a typical shear angle  $\beta = 50^\circ$  and azimuthal angle  $\theta = 85^\circ$  (configuration (i)), particles entering from above the sheet (assuming positive  $B_n$ ) often experience significant pitch-angle jumps or strong diffusion. In contrast, particles entering from below the sheet typically undergo minimal pitch-angle changes. Occasionally, interactions with current sheets having very large shear angles ( $\beta$ , e.g., configuration (ii)) or smaller azimuthal angles ( $\theta$ , e.g., configuration (iii)) result in enhanced diffusion and the reflection of certain particles from the current sheet, indicated by a reversal in the sign of  $\cos \alpha$ . For high-energy particles, interactions with current sheets of comparable

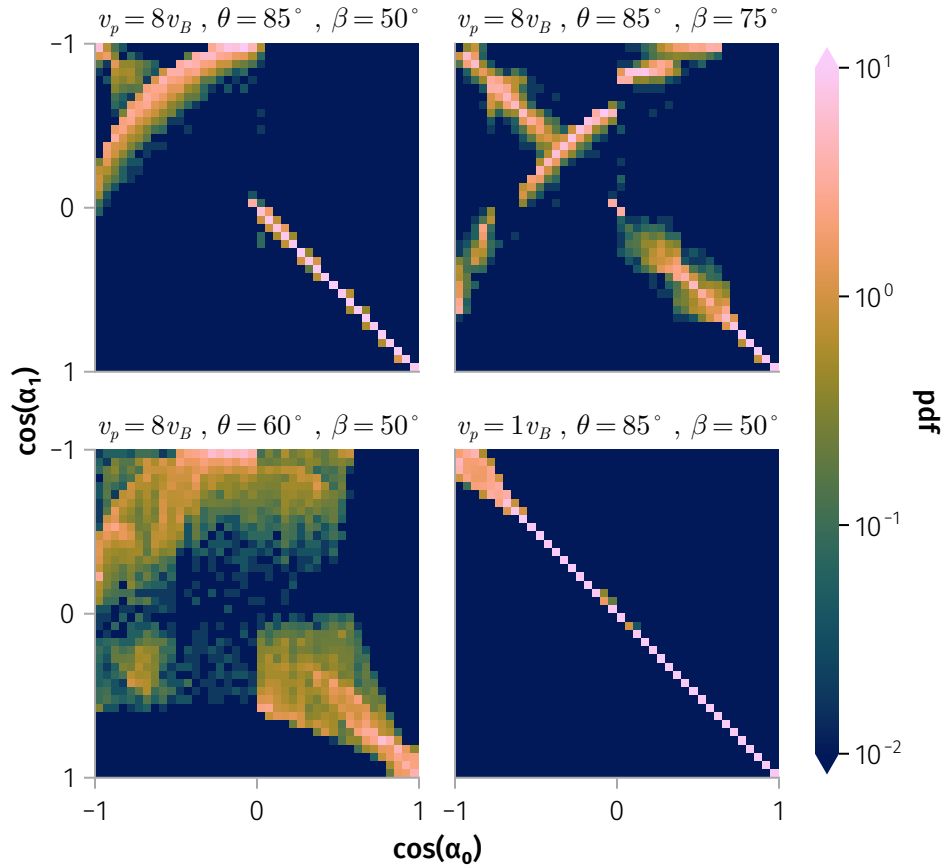


Figure 6: Transition matrix for 100 keV protons under four distinct magnetic field configurations:  
 (i)  $v_p = 8v_0$ ,  $\theta = 85^\circ$ ,  $\beta = 50^\circ$ ; (ii)  $v_p = 8v_0$ ,  $\theta = 85^\circ$ ,  $\beta = 75^\circ$ ;  
 (iii)  $v_p = 8v_0$ ,  $\theta = 60^\circ$ ,  $\beta = 50^\circ$ ; and (iv)  $v_p = v_0$ ,  $\theta = 85^\circ$ ,  $\beta = 50^\circ$ .

characteristic speed ( $v_0 \sim v_p$ , configuration (iv)) are rare, with scattering occurring only weakly and over a narrow range of pitch angles. The interplay between non-diffusive jumps and continuous diffusive processes drives a dynamic evolution of the particle ensemble. Over time, this leads to a broadened and redistributed pitch-angle profile, reflecting the statistical nature of interactions with solar wind current sheets.

## Long-term pitch angle evolution

Long-term modeling of particle pitch-angle distributions resulting from current-sheet scattering involves simulating the dynamics of a large number of particles through multiple current-sheet interactions over extended periods. To reduce computational time and complexity, we derive a simplified probabilistic description of pitch-angle evolution for modeling energetic particle transport under current-sheet scattering. The scattering process depends on the particle's initial conditions,  $(\mathbf{r}, \mathbf{v})$ , as well as the configuration of the current sheet,  $\mathbf{B}$ . In the 1D model, these initial conditions can be expressed in terms of  $z, E_0, \alpha_0$ , and  $\psi_0$ . Since our primary interest lies in the pitch angle after the particle exits the current sheet, and the energy  $E_0$  remains constant in the absence of an electric field, the initial energy  $E_0$  and position  $z$  (provided the particle is sufficiently far from the center of the current sheet) can be omitted from further consideration.

The final pitch angle, however, is highly sensitive to initial conditions  $(\alpha_0, \psi_0)$ , where small variations in the gyro phase can lead to significantly different final pitch angles [Malara et al., 2021]. Therefore, the scattering process  $\Pi : (\alpha_0, \psi_0) \rightarrow (\alpha_1, \psi_1)$  is better represented as a probabilistic transition  $p(\alpha_1 | \alpha_0, \Pi)$ , with the probability derived through numerical interpolation of the transition matrix. Here,  $\Pi$  characterizes the current sheet configuration. This probabilistic representation is further justified by the fact that the gyro phase depends on the particle's location and may undergo random shifts during the crossing of a current sheet. Additionally, numerical integration methods, such as the Boris method, introduce a phase error proportional to  $\Delta t$ , making the gyro phase less reliable. Thus, it is more appropriate to model the gyro phase as a random variable. This probabilistic approach eliminates the dependence on the gyro phase, instead focusing on the statistical relationship between the initial pitch angle  $\alpha_0$  and the final pitch angle  $\alpha_1$ , as governed by the properties of the current sheets.

For particles with a specific energy, a weighted transition matrix (WTM) can be constructed over the observed distribution of SWDs:  $p(\alpha_1 | \alpha_0) = \sum_i p(\alpha_1 | \alpha_0, \Pi_i) w_i$ , where the weight  $w_i$  corresponds to the occurrence probabilities of specific SWD configurations. The WTM accounts for the varying likelihoods of particles encountering SWDs with different properties and encapsulates the overall probability of a particle undergoing a pitch-angle jump at 1 AU due to interactions with an ensemble of SWDs.

As illustrated in Figure 7, the WTM for 100 keV protons at 1 AU shows a strong likelihood of minimal pitch-angle changes, evidenced by the bright diagonal. Additionally, it highlights significant probabilities associated with diffusive scattering, alongside a non-negligible likelihood

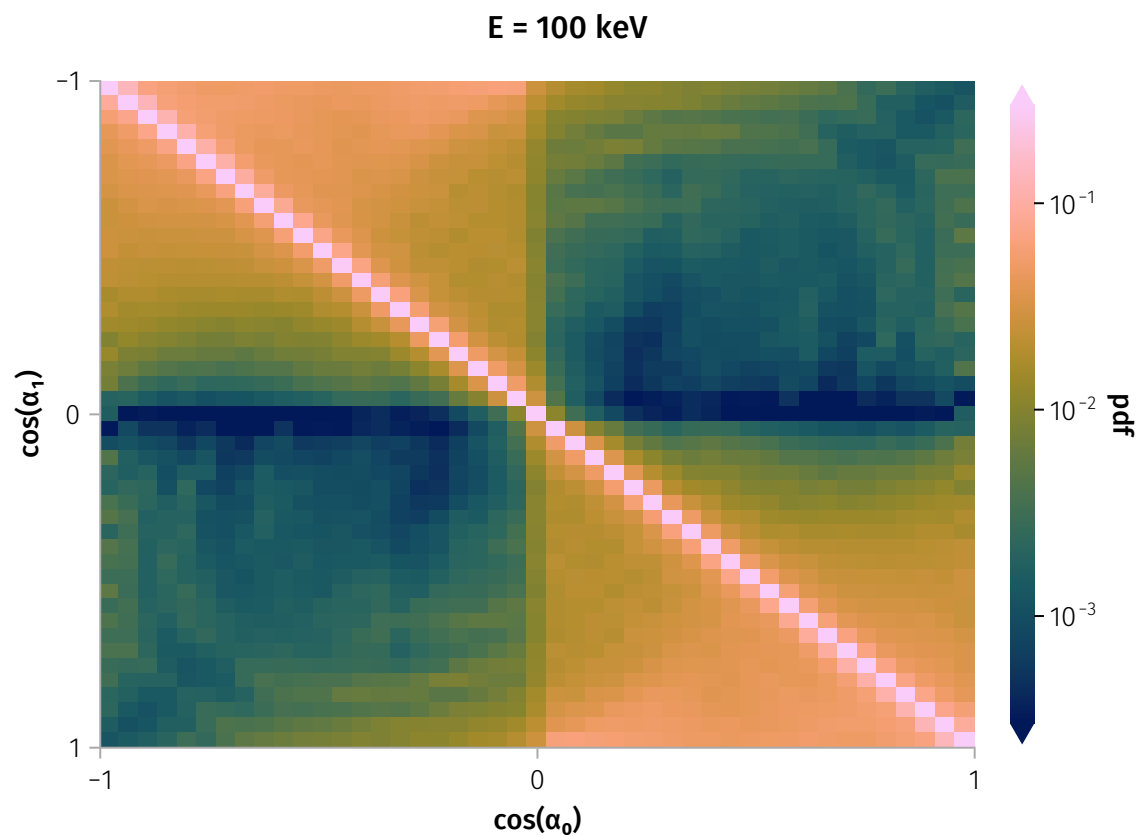


Figure 7: Weighed transition matrix for 100 keV particles constructed from the observed distribution of current sheet at 1 AU.

of large pitch-angle changes. These large-angle jumps mainly arise from interactions with current sheets whose characteristic scales ( $L$ ) are comparable to or smaller than the gyroradius of 100 keV protons. Such strong scattering cannot be adequately described by diffusion alone. However, the stochastic difference equations described in Equation 1 allow direct application of the WTM to simulate the long-term evolution of particle pitch-angle distributions:

$$\alpha_{n+1,i} = W(\alpha_{n,i}, \xi_{n,i}) \quad (1)$$

where  $n$  is the number of interaction (interaction with SWD),  $i$  is the particle index within the ensemble, and  $W(\alpha_{n,i}, \xi_{n,i})$  determines pitch-angle change from the WTM and a given random variable  $\xi_{n,i}$ , which is sampled from a uniform distribution.

Figure 8 illustrates two representative solutions of the dynamical pitch-angle mapping equation derived from the WTM at 1 AU for 100 keV and 1 MeV protons. A key feature of the pitch-angle dynamics is the occurrence of infrequent but substantial jumps, including rare, large-angle changes that can lead to particle reflection from the current sheet.

However, directly incorporating stochastic difference equations and the WTM into classical numerical schemes for transport-diffusion equations is a complex task. To facilitate comparison with other scattering processes and enable the inclusion of SWD-induced scattering effects in such models, we evaluate the effective scattering rate,  $D_{nn}$ . This rate acts as a global diffusion coefficient, independent of the local pitch angle, since high-energy particles frequently experience large pitch-angle jumps, leading to strong mixing. The scattering rate depends on the particle energy and the WTM (i.e., the distribution of current sheets). Using the mapping described in Equation 1 for an ensemble of particles, we calculate the evolution of the second moment of the pitch-angle distribution for the ion energy range from 100 keV to 1 MeV for current sheets at 1 AU:

$$\begin{aligned} M_1(n) &= N^{-1} \sum_{i=1}^N (\alpha_{n,i} - \alpha_{0,i}) \\ M_2(n) &= N^{-1} \sum_{i=1}^N (\alpha_{n,i} - \alpha_{0,i})^2 - M_1^2(n) \end{aligned}$$

where  $M_1(n)$  represents the mean shift in pitch angle, and  $M_2(n)$  quantifies the spreading in pitch angle. The function  $M_2(n)$  increases linearly with the number of interactions with current sheets before reaching saturation, where the pitch-angle distribution is adequately mixed. This behavior is illustrated in Figure 9.

We fit  $M_2(n)$  using an exponential model,  $M_2(n) = c - ae^{-D_{nn}n}$ , where  $c$  is the saturated second moment and  $a$  is the slope of the exponential fit. The derived scattering rates are analogous to diffusion coefficients for pitch-angle scattering and can be directly incorporated into transport-diffusion simulations. This approach provides a simplified yet effective means to account for current-sheet-induced scattering in broader models of energetic particle dynamics.

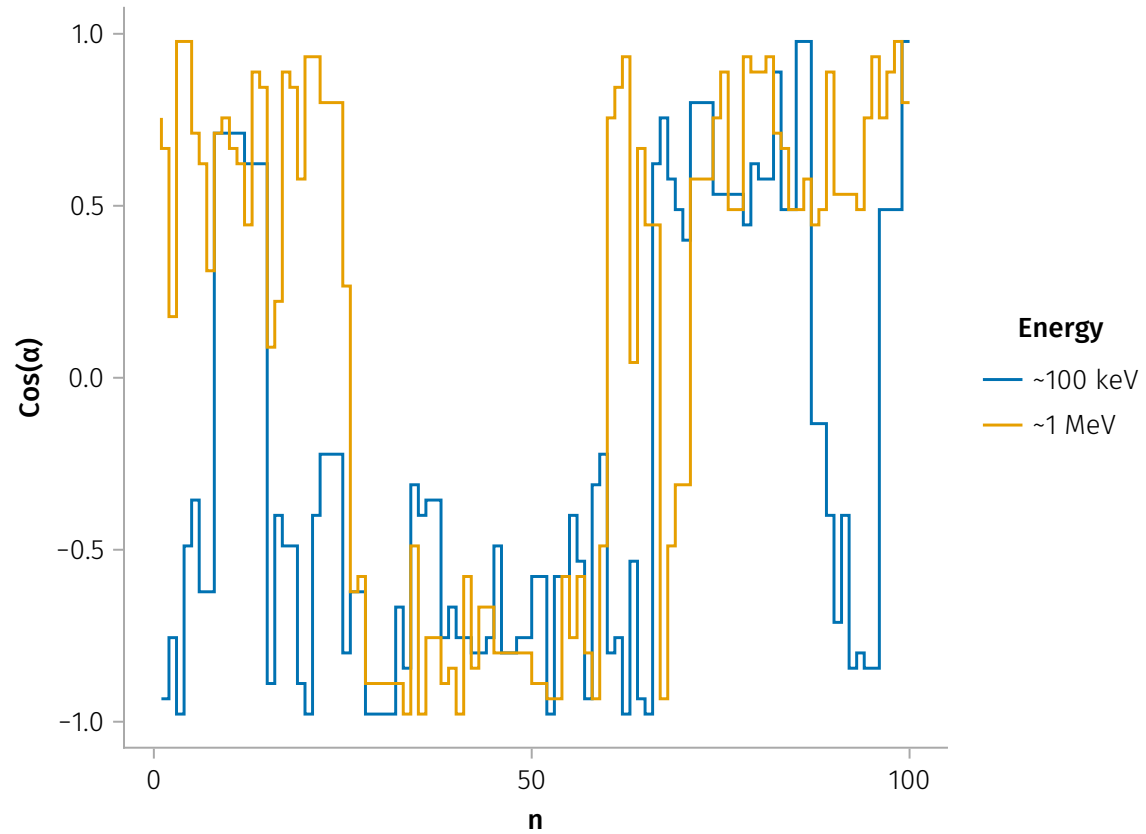


Figure 8: Examples of ion pitch angle scattering by solar wind discontinuities for 100 keV and 1 MeV protons.

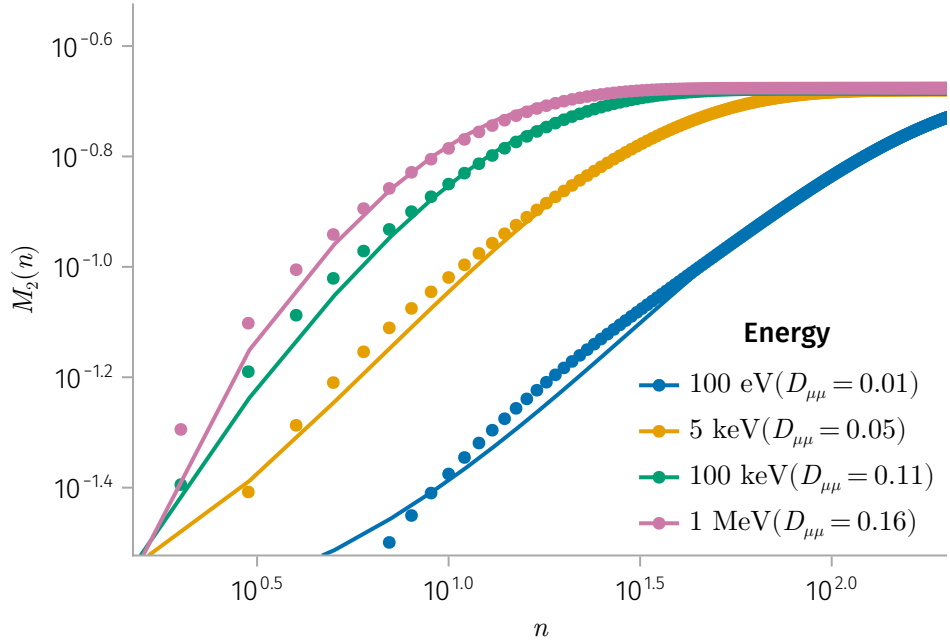


Figure 9: Mixing rates of particles as a function of interaction number ( $n$ ) for different particle energies ( $\sim 100$  eV,  $\sim 5$  keV,  $\sim 100$  keV,  $\sim 1$  MeV). The mixing rate is characterized by the second moment of the pitch-angle distribution,  $M_2(n)$ , quantifying the spreading of particles in pitch-angle space.

## Conclusion

In this study, we have investigated the scattering of energetic particles by current sheets and developed a model that incorporates the rotational effects  $\beta$ , the magnetic field magnitude, and the current sheet thickness  $L$ . Our findings indicate that current sheets characterized by large rotation angles or relatively small characteristic velocities, defined as  $v_0 = \frac{qB_0L}{cm}$ , can effectively scatter energetic particles. These scattering effects go beyond the conventional diffusion framework, as large pitch-angle jumps lead to rapid particle mixing. Leveraging extensive observations of solar wind current sheets at 1 AU, we have provided a statistical estimate that quantifies the long-term scattering rate of energetic particles due to current sheets.

In the heliosphere, the magnetic field strength decreases approximately with radial distance as  $\sim 1/r$ , while the current sheet thickness scales with the ion inertial length, which increases with radial distance. Consequently, the characteristic velocity  $v_0$  remains nearly constant with radial distance, indicating that energetic particles will continue to experience significant scattering by current sheets as they propagate through the heliosphere. The higher occurrence rate of current sheets closer to the Sun implies an even more pronounced impact on the transport of solar energetic particles.

These findings have significant implications for the dynamics of energetic particles in both space and astrophysical plasmas. Efficient pitch-angle scattering plays a crucial role in particle transport parallel to the magnetic field, as the parallel spatial diffusion coefficient is inversely proportional to the pitch-angle diffusion coefficient. Enhanced pitch-angle scattering, therefore, leads to shorter acceleration timescales in diffusive shock acceleration mechanisms. Observations frequently reveal broad spatial distributions of solar energetic particles and the formation of particle reservoirs [Cohen et al., 2021], suggesting either reduced diffusion rates along magnetic field lines or highly efficient cross-field diffusion [Zhang et al., 2009]. The influence of current sheets on parallel and perpendicular transport will be addressed in future work.

## Data availability

The code and data used for the findings and figures in this study are available at [https://github.com/Beforerr/ion\\_scattering\\_by\\_SWD](https://github.com/Beforerr/ion_scattering_by_SWD). ARTEMIS and Wind data are available at NASA's Space Physics Data Facility (SPDF) <https://spdf.gsfc.nasa.gov>.

## References

- V. Angelopoulos. The ARTEMIS Mission. *Space Science Reviews*, 165(1):3–25, December 2011.  
ISSN 1572-9672. doi: 10.1007/s11214-010-9687-2.

- A. V. Artemyev, A. I. Neishtadt, A. A. Vasiliev, V. Angelopoulos, A. A. Vinogradov, and L. M. Zelenyi. Superfast ion scattering by solar wind discontinuities. *Physical Review E*, 102(3):033201, September 2020. doi: 10.1103/PhysRevE.102.033201.
- H. U. Auster, K. H. Glassmeier, W. Magnes, O. Aydogar, W. Baumjohann, D. Constantinescu, D. Fischer, K. H. Fornacon, E. Georgescu, P. Harvey, O. Hillenmaier, R. Kroth, M. Ludlam, Y. Narita, R. Nakamura, K. Okrafka, F. Plaschke, I. Richter, H. Schwarzl, B. Stoll, A. Valavanoglou, and M. Wiedemann. The THEMIS fluxgate magnetometer. *Space Science Reviews*, 141(1):235–264, December 2008. ISSN 1572-9672. doi: 10.1007/s11214-008-9365-9.
- Christina M. S. Cohen, Gang Li, Glenn M. Mason, Albert Y. Shih, and Linghua Wang. Solar Energetic Particles. In *Solar Physics and Solar Wind*, chapter 4, pages 133–178. American Geophysical Union (AGU), 1 edition, 2021. ISBN 978-1-119-81560-0. doi: 10.1002/9781119815600.ch4.
- Elisa De Giorgio, Sergio Servidio, and Pierluigi Veltri. Coherent structure formation through nonlinear interactions in 2D magnetohydrodynamic turbulence. *Scientific Reports*, 7(1):13849, October 2017. ISSN 2045-2322. doi: 10.1038/s41598-017-13943-7.
- Mihir Desai and Joe Giacalone. Large gradual solar energetic particle events. *Living Reviews in Solar Physics*, 13(1):3, September 2016. ISSN 1614-4961. doi: 10.1007/s41116-016-0002-5.
- Richard Durrett. *Essentials of Stochastic Processes*. Springer Texts in Statistics. Springer International Publishing, Cham, 2016. ISBN 978-3-319-45613-3 978-3-319-45614-0. doi: 10.1007/978-3-319-45614-0.
- J. Giacalone and J. R. Jokipii. The transport of cosmic rays across a turbulent magnetic field. *The Astrophysical Journal*, 520(1):204, July 1999. ISSN 0004-637X. doi: 10.1086/307452.
- M. A. Lee and L. A. Fisk. Shock acceleration of energetic particles in the heliosphere. *Space Science Reviews*, 32(1):205–228, March 1982. ISSN 1572-9672. doi: 10.1007/BF00225185.
- Y. Y. Liu, J. B. Cao, H. S. Fu, Z. Wang, Z. Z. Guo, and R. J. He. Failures of Minimum Variance Analysis in Diagnosing Planar Structures in Space. *The Astrophysical Journal Supplement Series*, 267(1):13, July 2023. ISSN 0067-0049. doi: 10.3847/1538-4365/acdd58.
- Francesco Malara, Silvia Perri, and Gaetano Zimbardo. Charged-particle chaotic dynamics in rotational discontinuities. *Physical Review E*, 104(2):025208, August 2021. doi: 10.1103/PhysRevE.104.025208.
- W. H. Matthaeus, G. Qin, J. W. Bieber, and G. P. Zank. Nonlinear collisionless perpendicular diffusion of charged particles. *The Astrophysical Journal*, 590(1):L53, May 2003. ISSN 0004-637X. doi: 10.1086/376613.
- M. Meneguzzi, U. Frisch, and A. Pouquet. Helical and nonhelical turbulent dynamos. *Physical Review Letters*, 47(15):1060–1064, October 1981. doi: 10.1103/PhysRevLett.47.1060.

- A.I. Neishtadt. On the Accuracy of Persistence of Adiabatic Invariant in Single-frequency Systems. *Regular and Chaotic Dynamics*, 5(2):213, 2000. ISSN 15603547, 14684845. doi: 10.1070/RD2000v005n02ABEH000143.
- D. Perrone, O. Alexandrova, A. Mangeney, M. Maksimovic, C. Lacombe, V. Rakoto, J. C. Kasper, and D. Jovanovic. Compressive coherent structures at ion scales in the slow solar wind. *Astrophysical Journal*, 826(2):196, July 2016. ISSN 0004-637X. doi: 10.3847/0004-637X/826/2/196.
- Denise Perrone, Roberto Bruno, Raffaella D'Amicis, Daniele Telloni, Rossana De Marco, Marco Stangalini, Silvia Perri, Oreste Pezzi, Olga Alexandrova, and Stuart D. Bale. Coherent events at ion scales in the inner heliosphere: Parker solar probe observations during the first encounter. *Astrophysical Journal*, 905(2):142, December 2020. ISSN 0004-637X. doi: 10.3847/1538-4357/abc480.
- F. Pucci, F. Malara, S. Perri, G. Zimbardo, L. Sorriso-Valvo, and F. Valentini. Energetic particle transport in the presence of magnetic turbulence: Influence of spectral extension and intermittency. *Monthly Notices of the Royal Astronomical Society*, 459(3):3395–3406, July 2016. ISSN 0035-8711. doi: 10.1093/mnras/stw877.
- Bengt U. Ö. Sonnerup and Maureen Scheible. Minimum and maximum variance analysis. *ISSI Scientific Reports Series*, 1:185–220, January 1998.
- Kathryn Whitman, Ricky Egeland, Ian G. Richardson, Clayton Allison, Philip Quinn, Janet Barzilla, Irina Kitiashvili, Viacheslav Sadykov, Hazel M. Bain, Mark Dierckxsens, M. Leila Mays, Tilaye Tadesse, Kerry T. Lee, Edward Semones, Janet G. Luhmann, Marlon Núñez, Stephen M. White, Stephen W. Kahler, Alan G. Ling, Don F. Smart, Margaret A. Shea, Valeriy Tenishev, Soukaina F. Boubrahimi, Berkay Aydin, Petrus Martens, Rafal Angryk, Michael S. Marsh, Silvia Dalla, Norma Crosby, Nathan A. Schwadron, Kamen Kozarev, Matthew Gorby, Matthew A. Young, Monica Laurenza, Edward W. Cliver, Tommaso Alberti, Mirko Stumpo, Simone Benella, Athanasios Papaioannou, Athanasios Anastasiadis, Ingmar Sandberg, Manolis K. Georgoulis, Anli Ji, Dustin Kempton, Chetraj Pandey, Gang Li, Junxiang Hu, Gary P. Zank, Eleni Lavasa, Giorgos Giannopoulos, David Falconer, Yash Kadadi, Ian Fernandes, Maher A. Dayeh, Andrés Muñoz-Jaramillo, Subhamoy Chatterjee, Kimberly D. Moreland, Igor V. Sokolov, Ilia I. Roussev, Aleksandre Taktakishvili, Frederic Effenberger, Tamas Gombosi, Zhenguang Huang, Lulu Zhao, Nicolas Wijsen, Angels Aran, Stefaan Poedts, Athanasios Kouloumvakos, Miikka Paassilta, Rami Vainio, Anatoly Belov, Eugenia A. Eroshenko, Maria A. Abunina, Artem A. Abunin, Christopher C. Balch, Olga Malandraki, Michalis Karavolos, Bernd Heber, Johannes Labrenz, Patrick Kühl, Alexander G. Kosovichev, Vincent Oria, Gelu M. Nita, Egor Illarionov, Patrick M. O'Keefe, Yucheng Jiang, Sheldon H. Fereira, Aatiya Ali, Evangelos Paouris, Sigiava Aminalragia-Giamini, Piers Jiggens, Meng Jin, Christina O. Lee, Erika Palmerio, Alessandro Bruno, Spiridon Kasapis, Xiantong Wang, Yang Chen, Blai Sanahuja, David Lario, Carla Jacobs, Du Toit Strauss, Ruhann Steyn, Jabus van den Berg, Bill Swalwell, Charlotte Waterfall, Mohamed Nedal, Rositsa Miteva, Momchil Dechev, Pietro Zucca, Alec Engell, Brianna Maze, Harold

Farmer, Thuha Kerber, Ben Barnett, Jeremy Loomis, Nathan Grey, Barbara J. Thompson, Jon A. Linker, Ronald M. Caplan, Cooper Downs, Tibor Török, Roberto Lionello, Viacheslav Titov, Ming Zhang, and Pouya Hosseinzadeh. Review of solar energetic particle prediction models. *Advances in Space Research*, 72(12):5161–5242, December 2023. ISSN 0273-1177. doi: 10.1016/j.asr.2022.08.006.

Ming Zhang, Gang Qin, and Hamid Rassoul. Propagation of Solar Energetic Particles in Three-Dimensional Interplanetary Magnetic Fields. *The Astrophysical Journal, Volume 692, Issue 1, pp. 109-132 (2009).*, 692(1):109, February 2009. ISSN 0004-637X. doi: 10.1088/0004-637X/692/1/109.